STRUCTURE OF THE HYDROTHERMAL ROOT ZONE OF THE SHEETED DIKES IN FAST-SPREAD OCEANIC CRUST: A CORE-LOG INTEGRATION STUDY OF ODP HOLE 1256D, EASTERN EQUATORIAL PACIFIC

Marie Violay*,✉, Philippe A. Pezard, Benoit Ildefonse, Bernard Célérier and **Agathe Deleau**

Géosciences Montpellier, Université Montpellier 2, - CNRS, Montpellier, France.
* *now at INGV - Istituto Nazionale di Geofisica e Vulcanologia, Roma, Italy.*
✉ *Corresponding author, email: marie.violay@ingv.it*

ABSTRACT

Ocean Drilling Program Hole 1256D reached for the first time the transition zone between the sheeted dike complex and the uppermost gabbros. The recovered crustal section offers a unique opportunity to study the deepest part of the hydrothermal system in present-day oceanic crust. We present a structural analysis of electrical borehole wall images. We identified, and measured the orientations of four categories of structures: major faults, minor fractures, possibly hydrothermal veins, and dikes. All structures tend to strike parallel to the paleo-ridge axis. Three major fault zones (meter thick) and dikes are steeply dipping (~ 75° on average) outward the ridge. Centimeter-thick moderately conductive planar features are interpreted as hydrothermal veins, are organized in arrays of consistent spacing, thickness, and orientation, and are dipping about 15-20° toward the ridge. This structural pattern is interpreted as an on-axis paleo-hydrothermal circulation system, with vertical, dike-parallel fractures, and sub-horizontal high-temperature hydrothermal veins at the base of the sheeted dike, which was subsequently rotated ~ 15° westward around a ridge-parallel, sub-horizontal axis. This rotation can be caused by upper-crustal block rotation along a listric normal fault, and/or subsidence at the ridge axis.

INTRODUCTION

The mid-ocean ridge system is the largest continuous volcanic feature on Earth, with significant interactions between tectonic activity, volcanism and seawater circulation (e.g., Lister, 1974Macdonald, 1982). At mid-ocean ridges, new crust is formed, and rapidly cooled by hydrothermal circulation (e.g., Morton and Sleep, 1985; Morgan and Chen, 1993; Johnson et al., 1994; Stein and Stein, 1994). Seawater penetrates into the upper crust, and is heated as it moves down toward the base of the sheeted dike complex, in the vicinity of the magma chamber. Hydrothermal fluids are discharged along the ridge axis at temperatures up to ~ 400°C (e.g., Koschinsky et al., 2008). While circulating in the upper crust, seawater reacts with basaltic rocks, and exchanges mass and heat (e.g., Edmond et al., 1982; Alt et al., 1996; 2010; Bach et al., 2003).

The 1522 m deep ODP Hole 1256D is the first and only scientific drill hole that drilled a complete section of upper oceanic crust, from extrusive lava through dikes and into a few tens of meters of underlying gabbros (Wilson et al., 2003; 2006; Teagle et al., 2006). It is located in the Guatemala Basin and penetrated the 15 Ma crust of the Cocos Plate, formed at the East Pacific Rise (EPR) during a period of superfast spreading rate (> 200 mm/yr). The paleo-ridge is currently oriented NW-SE (Fig. 1; Wilson, 1996; Wilson et al., 2006).

The drilled basement at Site 1256 consists, from top to bottom, of ~ 800 m thick alternating thin sheet, massive and pillow lava flows, a ~350 m thick sheeted dike complex, and a ~ 100 m thick zone of transition to the lower crust, which is composed of two distinct gabbro intervals screened by granoblastic dikes (Fig. 2; Teagle et al., 2006; 2012).

This first complete penetration of the upper oceanic crust to the uppermost gabbros offers a unique opportunity to study the deep part of the hydrothermal system, in the transition zone between the sheeted dike complex and the lower crust gabbro of present-day in situ oceanic crust (Fig. 3). The root zone of the sheeted dike complex represents a thin zone of extreme thermal gradient (Teagle et al., 2006; 2012; Alt et al., 2010), and can be regarded as a dynamic thermal boundary layer in the ocean crust between the magma chamber system (axial melt lens) below (1100°C) and the main convective hydrothermal system above (≤ 450°C) (e.g., Lister, 1980; Gillis, 2002; 2008; Koepke et al., 2008; 2011; France et al., 2009; Alt et al., 2010).
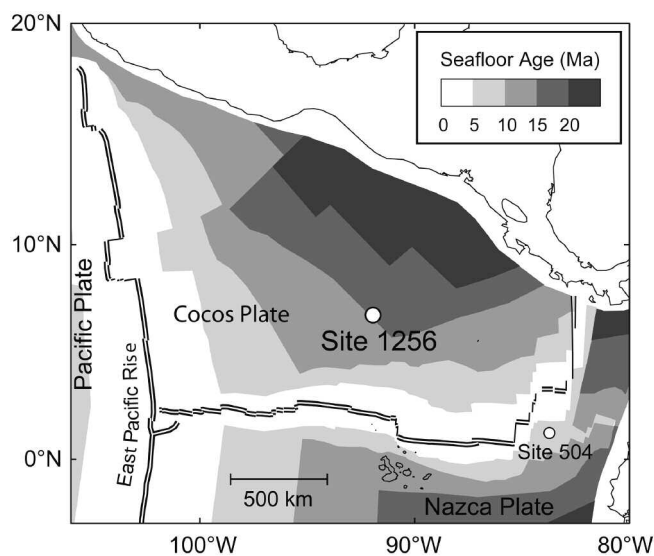

Fig. 1 - Location of ODP Site 1256 (modified from Teagle et al., 2006). The different gray areas are bounded by isochrones at 5 Ma intervals. The location of DSDP Site 504 is also shown.

ODP Hole 1256D

Division

Sedimentary overburden

Recovery (%)

0 50 100

Lithology

250

Lava pond

Inflated flows

500

Sheet and massive flows

Depth (mbsf)

1000

Transition zone

Sheeted dike complex

1250

investigated interval

Plutonic section

1500

Sheet flow

Massive basalt

Pillow basalt

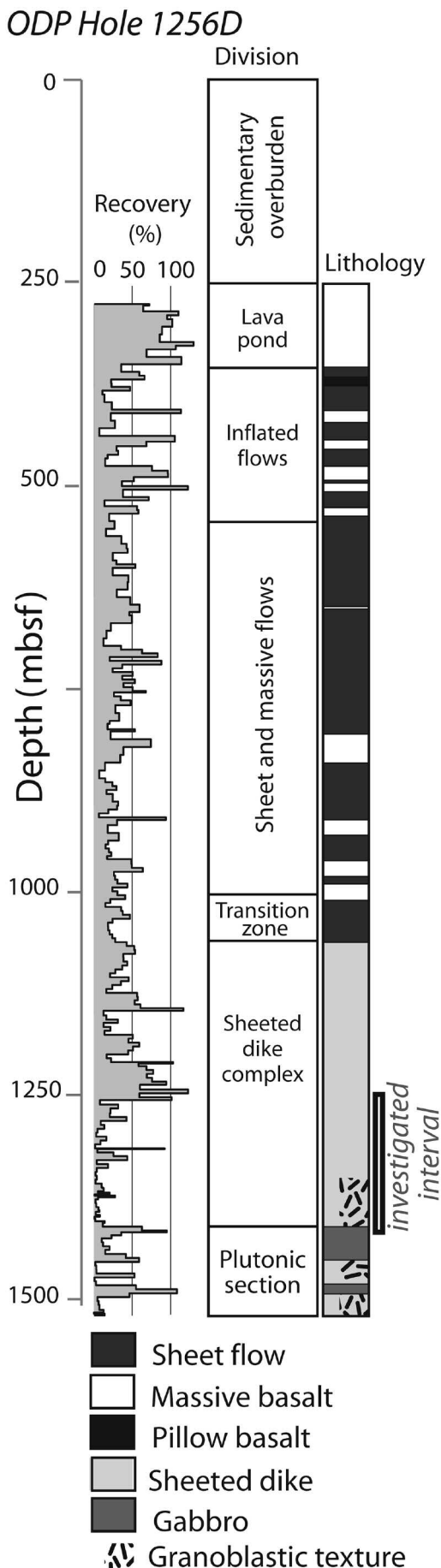Sheeted dike

Gabbro

Granoblastic texture

Fig. 2 - Summary of lithostratigraphy in Hole 1256D (after Teagle et al., 2012).

Logging ODP Hole 1256D with the Formation Micro Scanner (FMS) during IODP Expedition 312 (Teagle et al., 2006) provided continuous, oriented, high-resolution images in the root zone of the sheeted dikes down to 1437 meters below seafloor (mbsf), in the first gabbro interval.

FMS and core data are complementary to structural studies in many respects. Important detailed structures such as fractures, veins, or intrusive contacts are observed in core, but FMS images are oriented in space, whereas cores are not oriented in the horizontal plane. Moreover, core recovery is often incomplete (e.g., < 19% in the root zone of the sheeted dike complex; Teagle et al., 2006) and biased with respect to lithology or structures (e.g., fractured intervals are less recovered), whereas FMS images are continuous (Fig. 3). A preliminary analysis of Hole 1256D FMS data was done on board (Teagle et al., 2006). Tominaga et al. (2009) provide a detailed analysis of the electro-facies in ODP Hole 1256D, and interpret these facies in terms of volcanostratigraphy. Fontana et al. (2010) used FMS and other log data to depth shift and reorient core pieces in the shallow lava pond section of Hole 1256D.

In this study, we conducted a comprehensive structural analysis of the FMS images in the root zone of the hydrothermal system from 1250 mbsf to 1406 mbsf. We chose 1250 mbsf as the upper limit because it corresponds to a depth where non-granoblastic dikes are far above the zone of interactions between melt and hydrothermal fluids (i.e., the transition from granoblastic dikes to gabbro). FMS images can be analyzed down to 1406 mbsf; below 1407 mbsf the formation is very resistive, resulting in poor data quality (see section 3 below).

The main goal of the FMS structural analysis was to map and describe the structures in the root zone that could not be observed in cores, to characterize their organisation, to measure their orientation, and to tentatively relate them to the global scheme of hydrothermal circulation. We compare our results with downhole geophysical measurements (Guérin et al., 2008; Swift et al., 2008; Carlson, 2010; 2011; Violay et al., 2010; Gilbert and Salisbury, 2011), and petrological observations on cores collected during (Teagle et al., 2006) and after the cruise (Koepke et al., 2008; 2011; France et al., 2009; Alt et al., 2010). The petrological descriptions are used, whenever possible, to ascribe an origin to the structures mapped with the FMS.

METHODS

The FMS images of the borehole walls are generated from electrical conductivity measurements of the formation (e.g., Ekstrom et al., 1987; Pezard and Lovell, 1990). The FMS logging tool consists of four orthogonal pads that are in contact with the borehole wall, each containing 16 micro-electrodes. The slim version of the FMS tool used in ODP and IODP holes allows 22% coverage of the borehole wall surface (e.g., Ekstrom et al., 1987; Serra, 1989; Pezard and Lovell 1990; Tominaga et al., 2009). The image resolution is on the order of a few millimeters; any feature can be detected if its conductivity contrast with the matrix is sufficient. The electrical current intensity is recorded and converted to formation conductivity allowing the creation of an electrical image of the borehole wall. The color scale ranges from light colors for low conductivity to dark colors for high conductivity. A three components accelerometer and flux-gate magnetometer oriented
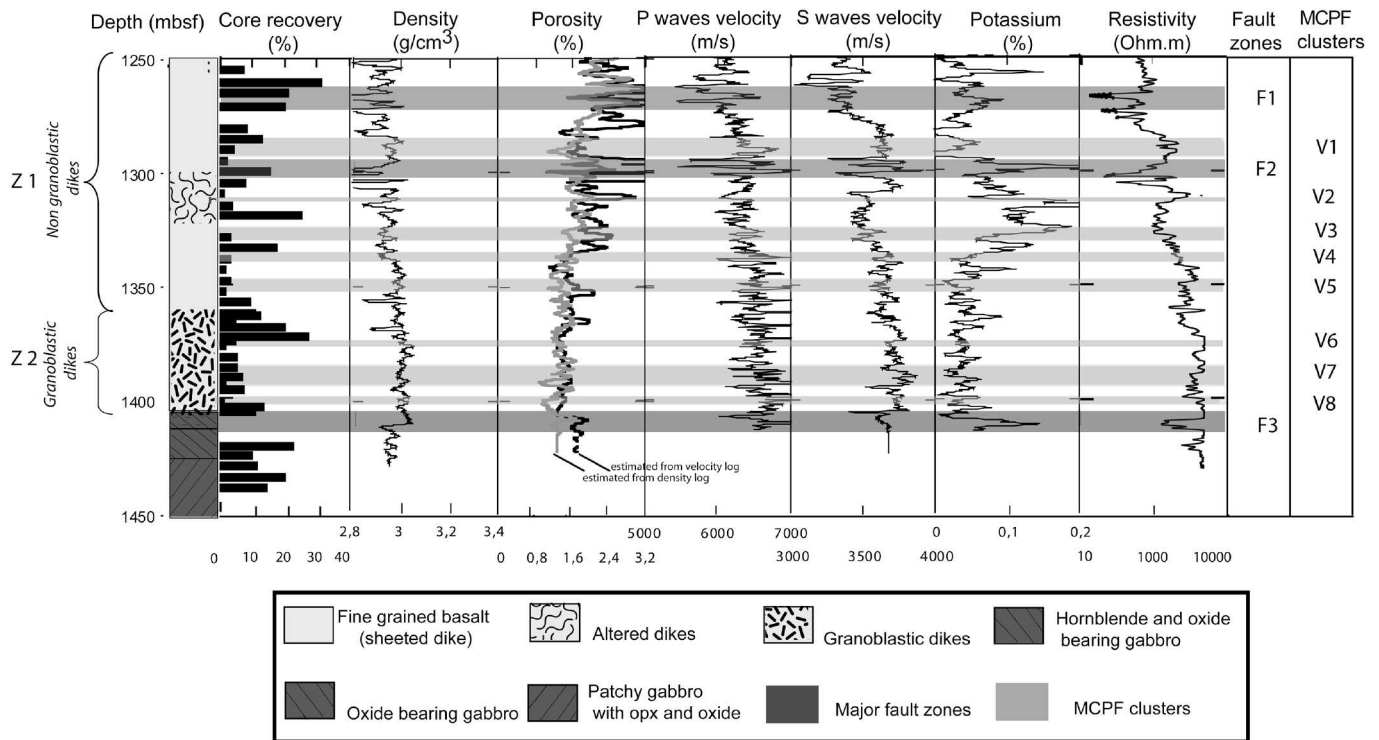
Fig. 3 - Downhole measurements in Hole 1256D between 1250 and 1450 mbsf. From left to right, density (from Teagle et al., 2006), porosity estimate from velocity and density logs (see Violay et al., 2010 for further explanations), P-wave velocity, S-wave velocity, potassium content and deep resistivity (from Teagle et al., 2006). The simplified lithostratigraphy of the root zone of the sheeted dike complex, the main faults zones, and the moderately conductive planar features (MCPF) clusters are also indicated.

the tool in space. Consequently, FMS images are oriented in the geographical reference frame, and allow one to determine the orientation (dip direction and dip) of detected planar features (e.g., Ayadi et al., 1998; Tartarotti et al., 1998; Fontana et al., 2010).

We analyzed FMS images using the Schlumberger software Geoframe 3.5 to obtain a set of interpreted structures. Planar structure orientations are measured on FMS images by fitting sinusoids to observed conductive features. The amplitude and phase of each sinusoid is converted into dip and dip direction. For each identified plane, the dip direction corresponds to the lower point on the sinusoid. The dip angle is calculated as $\tan^{-1}(H/R)$ where H is the amplitude of the sinusoid and R is the borehole radius (e.g., Ekstrom et al., 1987).The quality of FMS images recorded in Hole 1256D from two consecutive passes is excellent and recovered 22% to 44% of the borehole circumference down to 1407 mbsf. Below 1407 mbsf the formation is very resistive, resulting in poor data quality. The large resistivity contrast between the conductive fluid in the borehole and the resistive formation led to saturation of the FMS images. Consequently, the structures below 1406 mbsf are not identifiable, and the uppermost gabbros that were recovered from 1407 mbsf cannot be analyzed.

Porosity, density, electrical resistivity, acoustic velocities, and natural gamma rays have also been determined from downhole measurements in Hole 1256D and are here utilized for comparison with FMS structural data (Fig. 3; Teagle et al., 2006; Swift et al., 2008; Guérin et al., 2008; Tominaga et al., 2009; Carlson et al., 2010; 2011; Violay et al., 2010; Gilbert and Salisbury, 2011).

LITHOSTRATIGRAPHIC DESCRIPTION OF THE STUDIED ZONE (1250 TO 1407 MBSF)

The studied 1250 to 1407 mbsf interval may be subdivided in 2 lithostratigraphic zones, labeled Z1 and Z2 (Fig. 3).

Z1 (1250-1348 mbsf) corresponds to non-granoblastic dikes. The primary assemblage in basaltic dikes is plagioclase, clinopyroxene, Fe-Ti oxides, and minor olivine. Significant but local textural heterogeneities (cryptocrystalline in dike margins, medium-grained with few large (~ 1 mm) phenocrysts in dike cores) are described (Wilson et al., 2006). Non-granoblastic dikes are characterized by the occurrence of greenschist and sub-greenschist minerals in both the groundmass and the veins.

Hydrothermal alteration is recorded by (Alt et al., 2010):

(1) background recrystallization; chlorite is a major alteration phase above 1300 mbsf, and amphibole becomes dominant below that depth;

(2) veins and alteration halos along veins; veins are about one millimeter thick, and their frequency is 30 veins per meter on average; chlorite, quartz, pyrite, chalcopyrite, actinolite, prehnite, laumontite, and calcite are the most common vein-filling minerals; halos around veins are 1 to 11 millimeters thick;

(3) highly altered patches around vugs;

(4) local sulfide mineralization in breccias, dike margins, and veins.

Z2 (1348-1406 mbsf) corresponds to the granoblastic dikes. From 1348.3 to 1406.6 mbsf, the dikes are strongly to completely altered, and locally recrystallized to granoblastic textures (Teagle et al., 2006; Koepke et al., 2008; France et

al., 2009; Alt et al., 2010). Granoblastic dikes have the same primary mineral assemblages as non-granoblastic ones, but also display irregularly distributed granoblastic patches, with small-grained (~ 10 to 50 μm), granular, secondary clinopyroxene, plagioclase, magnetite ilmenite, and rare orthopyroxene. The recrystallized patches are ~ 0.5-1 mm in diameter. The granoblastic texture is interpreted as resulting from a metamorphic overprint due to the vicinity either of a gabbroic sill intrusion (Wilson et al., 2006) or of the axial melt lens itself (Koepke et al., 2008; France et al., 2009). It becomes more prominent at the bottom of the hole, where 100% recrystallized, granoblastic basalts have been recovered (Teagle et al., 2012). Hydrothermal alteration that postdates granoblastic recrystallization produces two types of veins. The first type consists of one-millimeter thick felsic veins that contain quartz, plagioclase, minor amphibole, and FeTi oxides. The second type of vein consists of one-millimeter thick Mg-hornblende and actinolite veins (Alt et al., 2010).

RESULTS

Electrical conductivity is a function of 1) pore fluid characteristics (primarily temperature and salinity), 2) porosity and geometry of the porous space, and 3) alteration (e.g., Waxman and Smits, 1968; Pezard, 1990; Revil and Glover, 1998; Ildefonse and Pezard 2001). Consequently, the variability of electrical conductivity, as recorded on FMS images, is related to changes of one or more of these parameters. Over 1500 structures have been mapped twice, through two distinct measurement sessions, and both operators have found identical and consistent results. The identified planes are organized into 3 main categories based on their conductivity (Fig. 4).

(**1**) Non-cemented fractures filled by seawater appear dark on FMS images, due to their high conductivity (Fig. 4a). They are divided into two sub-categories depending on their thickness: major fault zones are > 1 meter thick, and are clusters of many conductive structures. Minor fractures are typically < 10 centimeter thick. Major fault zones significantly impact downhole geophysical measurements, and correspond to an enlargement in the caliper record, in contrast with minor fractures (Fig 3).

(**2**) Moderately conductive planar features (MCPF) appear brown on FMS images (Fig. 4b). They are less conductive than non-cemented fractures (see above), but more conductive than the matrix. We posit that these structures are petrologically distinct from the background formation. We tentatively interpret them as hydrothermal veins (i.e., cemented fractures) with or without alteration halos. Their higher conductivity indicates that they contain more conductive phases than the matrix such as hydrous (chlorite, amphibole, smectite, zeolite…), or metallic (oxide) minerals. The exact mineralogy of these presumed veins is impossible to determine because they have not been recovered (see further discussion).

(**3**) Dikes (Fig. 4c) are sandwiched between pairs of large, blurred, parallel conductive planes on FMS images, which represent the altered dikes margins.

Each mapped planar feature is identified by its strike from 0 to 180°, its dip from 0 to 90°, and its dipping direction quadrant (E, S, N, W). Measurements are reported as N140 70E where 140 is the strike, 70 the dip and E the dip direction quadrant. The average orientation for each structural group was automatically computed using the Geoframe software.

Non cemented fractures

Major fault zones

Downhole geophysical measurements, borehole wall electrical images and core descriptions were used to identify three major fault zones labeled F1, F2, and F3 (Fig. 3). Note, however, that the recovery is very poor in these zones, and hence the core description was generally done on a series of small, rounded, non-oriented samples, some of which displaying a few breccias and/or fractures (Teagle et al., 2006).

F1 (1265-1273 mbsf) is located in lithostratigraphic zone Z1. Eighteen FMS fractures were mapped in this interval. F1 is oriented on average N140 70NE. Porosity increases from 2.5% outside the fault zone to more than 20% inside. Acoustic P and S wave velocities decrease from 6000 m/s to 5000 m/s, and from 3500 to 3200 m/s, respectively. F1 is also associated with a strong increase in potassium content related to alteration minerals such as clay and zeolite (Fig. 3; see also Violay et al., 2010). Breccias and non-granoblastic dikes, which bear secondary minerals such as chlorite, quartz, chalcopyrite and pyrite, are described in cores from this zone (Teagle et al., 2006; Alt et al., 2010). Such low temperature minerals are interpreted as early hydrothermal alteration at temperatures between 400°C and 300°C (Alt et al., 2010).

F2 (1296-1303 mbsf) is also within lithostratigraphic zone Z1. Seventeen fractures were mapped in this zone. F2 is oriented on average N160 60NE. High porosity (> 20%), high potassium value (> 0.1%) and low P-wave and S-wave velocities characterize this zone (Fig. 3, 4). As for F1, chlorite, quartz, chalcopyrite, and pyrite are abundant in recovered samples from this zone (Teagle et al., 2006; Alt et al., 2010).

F3 (1403-1404 mbsf) is located just a few meters above the boundary between granoblastic dikes and the upper gabbroic interval (at 1406.6 mbsf). F3 is oriented on average N150 70NE. It is also associated with a decrease in density and acoustic P and S wave velocity (from ~ 6500 m/s to ~ 6000 m/s, and from ~ 3800 m/s to ~ 3500 m/s, respectively), and with increased porosity (see Fig. 2). Hydrothermal alteration at temperature of 400-500°C in cores, marked by actinolite, chlorite, pyrite and magnetite, postdates the granulite metamorphism that is associated with granoblastic textures in granoblastic dikes (Teagle et al., 2006; Alt et al., 2010).

Minor fractures

Minor fractures with variable orientations are mapped in the entire root zone of the hydrothermal system. They mostly strike to the SE with moderate (15-35°) dip to the SW (Fig. 4b-c). They are on average perpendicular to the major fault zones (F1, F2, F3). They are more frequent in non-granoblastic dikes (~ 6-8 per meter) than in granoblastic dikes (~ 5-6 per meter).

Moderately conductive planar features (MCPF)

The MCPF that we interpret as possible hydrothermal veins are generally organized in clusters, always with consistent strikes and dips. Those that do not belong to a cluster mostly display a similar orientation. The average MCPF orientation is ~ N130 15-20 SW (Fig. 5). Their average thickness is about 1 cm, and the MCPF density in these clusters is 6 to 8 feature/meter. We have identified eight clusters labeled V1 to V8 (assuming MCPF are hydrothermal veins) in the mapped interval (Fig. 3): V1 from 1285 to 1295 mbsf, V2 from 1312 to 1313 mbsf, V3 From 1322 to 1329 mbsf, V4 from 1334 to 1337 mbsf, V5 from 1348 to 1351 mbsf,
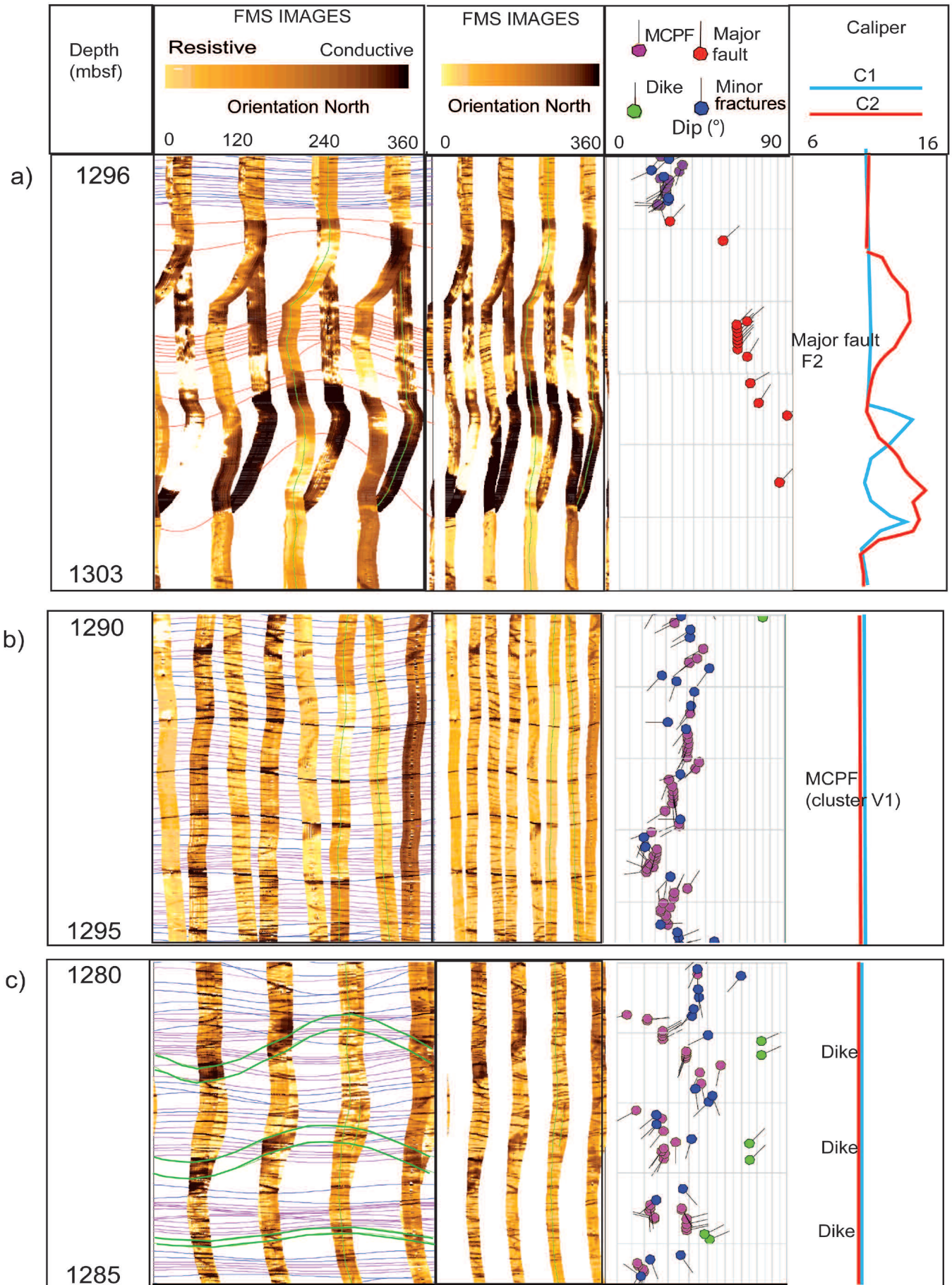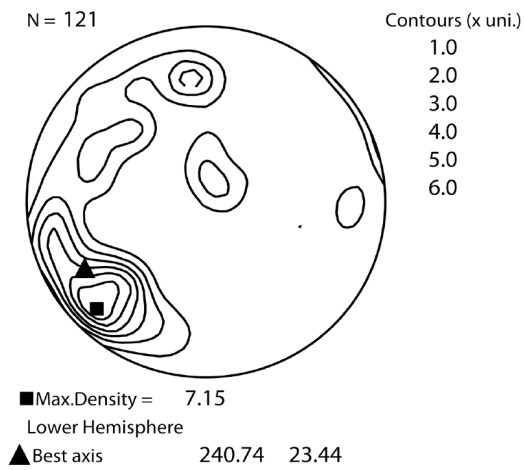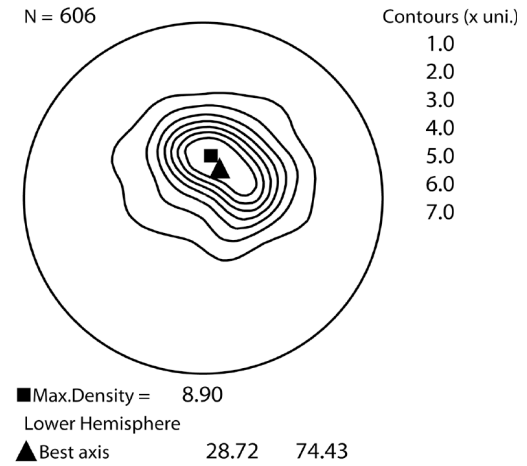
Fig. 4 - Example of FMS images of the major fault zone F2 (a), the MCPF cluster V1 (b), and dike boundaries (c). The position of the structure tadpoles (that correspond to the best-fit sinusoids on the FMS image) on the horizontal axis indicates the dip magnitude, and the tadpole tails point toward the dip direction.
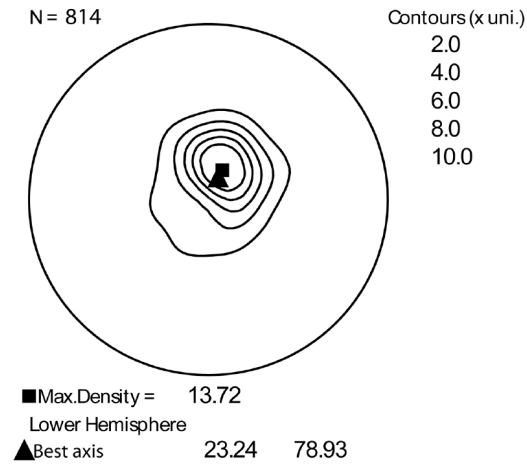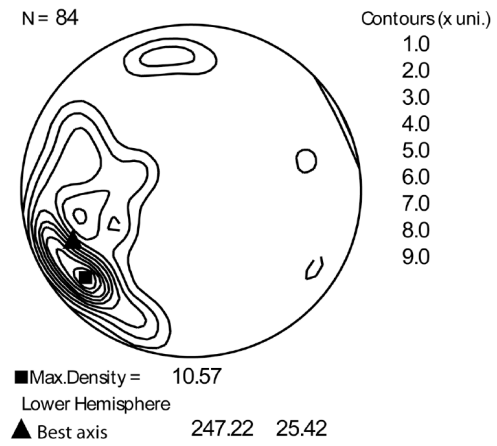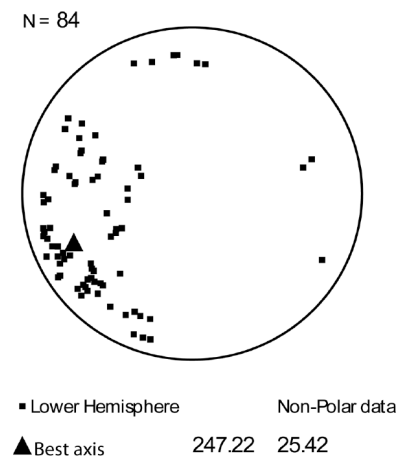
a) Fractures in fault zones.

N = 121

Contours (x uni.)
1.0
2.0
3.0
4.0
5.0
6.0

■ Max.Density =   7.15
Lower Hemisphere
▲ Best axis   240.74   23.44

b) Minor fractures

N = 606

Contours (x uni.)
1.0
2.0
3.0
4.0
5.0
6.0
7.0

■ Max.Density =   8.90
Lower Hemisphere
▲ Best axis   28.72   74.43

c) MCPF

N = 814

Contours (x uni.)
2.0
4.0
6.0
8.0
10.0

■ Max.Density =   13.72
Lower Hemisphere
▲ Best axis   23.24   78.93

d) Dikes

N = 84

Contours (x uni.)
1.0
2.0
3.0
4.0
5.0
6.0
7.0
8.0
9.0

■ Max.Density =   10.57
Lower Hemisphere
▲ Best axis   247.22   25.42

e) Dikes

N = 84

■ Lower Hemisphere   Non-Polar data

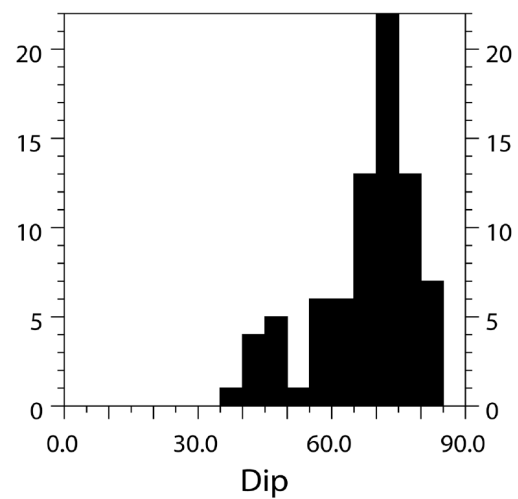▲ Best axis   247.22   25.42

f) Dikes

Dip

Fig. 5 - Equal area stereographic projection (lower hemisphere) of the poles of a) fractures in major fault zones, b) minor fractures, c) MCPF, and d-e) dike margins. In each stereographic projection, the indicated best axis is the first eigenvector of the corresponding orientation tensor. N is the number of measurements. Computations and plots are done with the program Field2K written by David Mainprice. f) Histogram of the dips of the dike margins.

V6 from 1374 to 1376 mbsf, V7 from 1387 to 1395 mbsf, and V8 from 1400 to 1402 mbsf. These 8 clusters unfortunately correspond to intervals of very low core recovery (< 5%; Fig. 3), in which most core pieces are too small (i.e., smaller than the core liner diameter) to be vertically oriented (see Visual Core Descriptions in Teagle et al., 2006). It is consequently impossible to compare the MCPF identified on FMS images with veins identified on the poorly recovered core from these intervals. Only a few veins were described, in generally non-oriented core pieces within the intervals where clusters V1 to V8 are mapped (Teagle et al., 2006; Alt et al., 2010). In V1 and V2, veins are about 1 millimeter thick, with maximum 7 millimeters thick halos, and filled with pyrite, quartz, and chlorite. In V3 and V4, they are infra-millimetric, and filled with sulfide, quartz, zeolite, chlorite and actinolite. In V5 and V6, they are infra-millimetric, and filled with quartz, zeolite, chlorite, and actinolite. In V7 and V8, they are filled with Mg-hornblende and actinolite.

The veins identified in core pieces are generally less than one millimeter thick, and generally display 0.1 to 10 mm thick halos. The resolution of FMS images being on the order of a few millimeters, it is impossible to see these veins in FMS data. No direct comparison can be made between the one millimeter thick veins observed on core pieces, and the ~ 1 cm thick MCPF identified on FMS Images. The few described veins in oriented core pieces are either sub-vertical or sub-horizontal (Teagle et al., 2006).

Dikes

Vertical dike margins were identified in both lithostratigraphic zones Z1 and Z2. Their downhole distribution is heterogeneous, with the highest density encountered between 1275 and 1290 mbsf. The average dike thickness ranges from 0.1 to 1 m. This is in good agreement with observations made on cores from the same interval (Teagle et al., 2006). Their average orientation is N165 75NE (Fig. 5), which is consistent with the average dip of dikes (~ 79°) in the whole dike complex (1060-1406 mbsf) measured on the same FMS images by Tominaga et al. (2009) and in recovered cores (Teagle et al., 2006).

DISCUSSION

All structures that are mapped and described in this study strike ~ N150 on average, which is sub-parallel to the paleo-ridge axis (Fig. 1; Hallenborg et al., 2003). MCPF and minor fractures dip to the west, towards the ridge axis, whereas major fault zones and dikes dip to the East, away from the ridge axis (Fig. 5). To simplify the discussion we call the former inward dipping structures and the latter outward dipping structures.

Hydrothermal conduits

Three types of structures were identified on the FMS images: major fault zones, minor fractures, and MCPF that we tentatively interpret as hydrothermal veins. All of these structures were potential conduits for hydrothermal fluid circulation at, or close to the ridge axis. We discuss here their on-axis or off-axis origin.

Major fault zones

F1, F2, F3 have consistent strikes and dips, which suggests that they were created in the same tectonic environment. Core recovery is very low in these fault zones. However, relatively low temperature alteration mineral assemblages (pyrite, chalcopyrite, chlorite, quartz) are observed in the breccias and dikes in core pieces recovered from fault zones F1 and F2, and middle temperature alteration mineral assemblages (actinolite, chlorite, magnetite) are described in the dike pieces recovered from fault zone F3 (Teagle et al., 2006; Alt et al., 2010). These alteration assemblages are interpreted as early hydrothermal alteration at temperatures between 450°C and 300°C (Alt et al., 2010). Consequently, although these faults may have been reactivated off-axis, an early, on-axis origin is very likely.

Outward dipping faults are not common in ocean crust formed at slow to intermediate spreading rates (e.g., Carbotte and Macdonald, 1990). As spreading rate increases, outward dipping faults become more abundant; at superfast rates (> 130 mm/yr, Francheteau and Ballard, 1983) outward dipping faults dominate (Carbotte and Macdonald 1990; 1994a). The outward dipping major fault zones in Hole 1256D are thus consistent with the superfast spreading environment of Site 1256.

Minor fractures

The minor fractures are perpendicular to the major fault zones and parallel to the less conductive MCPF. Small-scale fracture/crack systems in dikes have not been studied in great details, with the exception of fracture network descriptions in the sheeted dike complex of the Troodos ophiolite (Van Everdingen, 1995). Fractures are mm thick, and tend to be preferentially oriented either parallel or perpendicular to the dike margins. The fracture density varies from 1.1 to 4.7 fractures per meter, and decreases with depth. The orientation, thickness, and depth distribution of these fractures in the Troodos dikes are not completely consistent with those observed on the Hole 1256D FMS images. To our knowledge, sub-horizontal centimeter-thick fractures in the root zone of the sheeted dikes similar to those identified in Hole 1256D FMS images have not been described so far in cores or in ophiolites.

Fractures observed on FMS images may have formed by 1) thermal cooling (e.g., Shaefer and Kattenhorn, 2004), 2) on-axis seafloor tectonics, or 3) seafloor off-axis tectonics, as proposed by Gillis and Sapp (1997) for the effusive section of the Troodos Ophiolite in Cyprus.

MCPF

One of the main results of our FMS image analysis is the identification of clusters of MCPF, tentatively interpreted as hydrothermal veins, with consistent thickness (~ 1 cm), spacing, density and orientation (Figs. 4, 5). These clusters are unfortunately mapped in very low core recovery intervals (< 5%), and no direct comparison can be made between the FMS image and the core.

A very limited number of studies describe hydrothermal veins in the sheeted dikes of the root zone of the Oman and Troodos (Cyprus) ophiolites (Nehlig and Juteau, 1988; Nehlig, 1993; Nehlig et al., 1994; Gillis, 2002; Nicolas et al., 2008; France et al., 2009):

- Dense networks of epidote-quartz-sulfide bearing (< 450°C), millimeter thick veins have been observed at the base of the sheeted dike complex of the Oman ophiolite. About 90% of the veins are parallel to the dike margins; others are perpendicular (Nehlig et al., 1994). The density of these quartz-sulfide veins increases, whereas that of

epidote-quartz veins decreases (~ 0.5 veins/meter to 0.2 veins/meter) when approaching the dike/gabbro transition. Their dominant orientation, thickness, and density are not consistent with those observed on FMS images from ODP Hole 1256D.

- The occurrence of high temperature amphibole veins is reported in the root zone of the sheeted dikes in Oman (France et al., 2009), and in Cyprus (Gillis, 2002), but the lack of information on the vein thickness, spacing, and orientation hampers a direct comparison with the presumed vein set inferred from the studied FMS images. Amphibole veins and amphibole + chlorite veins have been studied by Tartarotti et al. (1995) in the lower part of the sheeted dike complex at ODP Hole 504B, above the root zone. These amphibole veins are mostly shallowly dipping, with only smaller peaks of steeply dipping orientation for the lower temperature chlorite and amphibole + chlorite-bearing veins.

To our knowledge, sub-horizontal consistent arrays of veins as those inferred from the FMS images analyzed herein have never been described in the field in the root zone of the sheeted dike. It is therefore impossible to assign an early or late origin to the MCPF that we interpret as hydrothermal veins. However, thinner (~ 1 mm) veins with 1 to 10 mm thick halos were found in non-oriented core pieces located just above or below these clusters. The alteration facies of these veins increases from zeolite to amphibolite facies with depth, from 1285 to 1402 mbsf (from V1 to V8). For example, Alt et al., (2010) describe, at 1382.19 mbsf close to cluster V7, a 1 mm thick Mg-hornblende + actinolite vein.

Assuming a hypothetical common origin of the millimeter thick veins observed on cores and centimeter thick MCPF observed on the FMS image, core observations suggest that at least V7 and V8 clusters could be related to high temperature hydrothermal circulation at or close to the ridge axis (Teagle et al., 2006; Alt et al., 2010) (see Fig. 6). The consistent strikes and dips of all measured MCPF clusters suggest that they might have been created in the same environment.

Rotation of mapped structures

The dike margins in the studied interval (1250-1406 mbsf) dip ~ 75° outward on average (Fig. 5). This is consistent with the average dip of dikes (~ 79°) in the whole sheeted dike complex (1060-1406 mbsf) measured on the same FMS images by Tominaga et al. (2009), and with average contact dips measured on cores (Teagle et al., 2006). This orientation suggests a modest rotation of about 10 to 15°, around a ridge-parallel sub-horizontal axis, assuming the dikes were originally vertical. The MCPF are interpreted as veins that possibly formed at the ridge axis. They are perpendicular to the dikes margins, which suggests that they underwent the same rotation, and were initially sub-horizontal (Fig. 5).

The sheeted dike complex formed in a fast-spreading context at the EPR is well described along the northern wall of the Hess Deep propagating rift (Karson et al., 1992; 2002a; 2002b; Hurst et al., 1994; Karson, 2002; Hurst and Karson, 2004). The dikes are rarely vertical, and most of them dip outward ~ 60°. Many faults are sub-parallel to dikes and also dip outward. The dips of the dikes at Hess Deep are significantly more dispersed and less steep on average than those observed at Site 1256.

Karson et al. (1992) proposed five alternative models for the generation of non-vertical dike swarms. In model 1 (Fig. 4a in Karson et al., 1992), the dip of the dikes decreases (i.e., rotation increases) in the vicinity of the magma chamber. The roof of the magma chamber is considered as a free surface that induces stress perturbation. In models 2 and 3 (Fig. 4b in Karson et al., 1992), the dikes rotate as a result of crustal block rotation along a listric normal fault; they dip inward in model 2, and outward in model 3. Model 4 explains the dike rotation by rapid axial subsidence of the upper crust (Fig. 4d in Karson et al., 1992). The effect of axial subsidence has also been described in lava flows in Iceland (Palmasson, 1973), and proposed at ODP site 504B (Pezard and Lovell, 1990). Subsidence rotates initially horizontal lava flows to inward dipping flows (Palmasson, 1973; Pezard and Lovell, 1990; Hooft et al., 1996). In model 5, the tilting
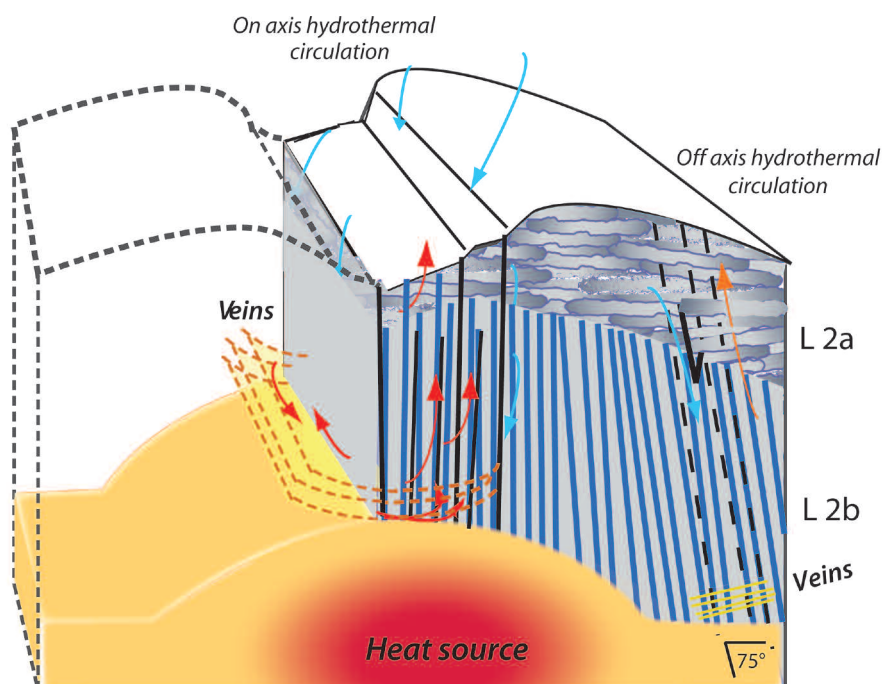

Fig. 6 - Conceptual sketch of the of the hydrothermal circulation system and associated structures in the upper crust (after the subsidence model (Model 4) of Karson et al., 1992). Yellow: MCPF, assumed to be hydrothermal veins that are formed sub-horizontal; solid black lines: on- axis hydrothermal fault, parallel to the sheeted dikes, dashed black lines: rotated fault, possibly reactivated outward dipping normal faults; red arrows: high temperature hydrothermal fluids; blue arrows: low temperature seawater fluids. L2a: effusive lava complex. L2b: sheeted dike complex.

of diabase dikes is not related to ridge axis processes, but results from rifting-related processes at Hess Deep.

Model 1 is not consistent with observations in Hole 1256D because dike orientation does not vary with depth. Model 5 is specific to the Hess Deep context, hence is not relevant to Site 1256. We can also exclude scenarios in which dikes dip inward (toward the ridge axis; i.e., model 2). Only models 3 and 4 can explain the outward dipping orientation of dikes at Site 1256. Model 3 is an appealing scenario for Hole 1256D because it explains both the rotation of dikes and presumed veins (assuming they were formed with sub-horizontal orientation and early enough to be rotated together with the dikes), as well as the outward dipping of the major fault zones if they reactivate pre-existing sub-vertical fractures parallel to the sheeted dikes at the ridge axis (Fig. 5). It requires normal faulting to accommodate block rotation; the mapped fault zones are possible candidate for such normal faulting. Outward dipping listric normal faults, though, are not seen in seismic reflection data around Site 1256, which reveal dominantly sub-horizontal reflectors in the flowline-parallel profiles (Hallenborg et al., 2003). Alternatively, a subsidence model (Model 4) could also explain the inward dipping of the dikes, and the presumed veins if these formed on-axis, prior to subsidence. Both models 3 and 4 are consistent with the relatively wide range of dike contact dips measured in both the FMS images and the recovered cores (~ 50 to 90°; Teagle et al., 2006), which may account for later vertical dikes cross-cutting older, rotated ones.

Using fault restoration technique of seafloor topography of the EPR at 18°14'S, Carbotte et al. (2003) demonstrate upper crustal rotation of ~ 15° at the ridge axis. This pattern is attributed to seafloor collapse at the ridge axis in the hanging walls of large master inward dipping faults, which flatten with depth (Carbotte and Macdonald, 1994a; 1994b; Bohnenstiehl and Carbotte, 2001; Carbotte et al., 2003). This collapse is related to the deflation of the shallow axial melt lens during eruptions that build the upper crust. This implies a rotation around a horizontal axis toward the ridge, which rotates initially horizontal lava flows to inward dipping flows, and initially vertical dikes to outward dipping dikes. This scenario roughly corresponds to model 4 of Karson et al. (1992). It can also explain the measured orientation of dikes, veins and major fault zones, and provides a mechanism for the rotation.

CONCLUSIONS

The main hydrothermal fluid conduits within the root zone of the hydrothermal circulation system at Site 1256, as identified on Hole 1256D FMS images, are a series of fractures, some of which defining three steeply dipping, meter-thick major fault zones that strike parallel to the paleo-ridge axis, and arrays of centimeter-thick MCPF interpreted as hydrothermal veins dipping 15-20° toward the ridge axis. Fault, dike, and vein orientations are represented in Fig. 6 in a conceptual model of hydrothermal circulation at the ridge axis and subsequent rotation due either to subsidence (e.g., Karson, et al., 1992; Carbotte et al., 2003) or to crustal block rotation along a listric normal fault (e.g., Karson et al., 1992). Major fault zones are outward dipping, consistent with observations at superfast segments of the EPR.

The origin of moderately inward dipping fractures, presumably originally sub-horizontal, is unclear as such features have not been described so far in cores or in ophiolites. They may be related to thermal cooling, and/or on-axis/off-axis seafloor tectonics.

The presumed vein arrays, which are also moderately dipping inward, and are perpendicular to the major fault zones and dike boundaries, may outline the deepest part of the on-axis hydrothermal system, but the geological structures associated to these moderately conductive, sub-horizontal FMS features cannot be conclusively characterized. Low recovery prevented the direct comparison between these features on FMS images and veins present in cores at the same depth. Further field studies should be carried out in ophiolites to look for similar, sub-horizontal (dike perpendicular) clusters of veins close to the base of the sheeted dike complex.

Structure orientations suggest a ~ 10 to 15° westward rotation around a ridge-parallel horizontal axis. This rotation is possibly related to subsidence due to volcanic collapse following lava eruption, i.e., melt lens deflation at the ridge axis, and/or to crustal block rotation along-outward dipping listric normal faults.

ACKNOWLEDGEMENTS

REFERENCES

Alt J.C., Laverne C., Coggon R.M., Teagle D.A.H., Banerjee N.R., Morgan S., Smith-Duque C.E, Harris M. and Galli L., 2010. Subsurface structure of a submarine hydrothermal system in ocean crust formed at the East Pacific Rise, ODP/IODP Site 1256. Geochem. Geophys. Geosyst., 11, Q10010, doi:10.1029/2010GC003144.

Alt J.C., Laverne C., Vanko D.A., Tartarotti P., Teagle D.A.H., Bach W., Zuleger E., Erzinger J., Honnorez J., Pezard P.A., Becker K., Salisbury M.H. and Wilkens R.H., 1996. Hydrothermal alteration of a section of upper oceanic crust in the eastern equatorial Pacific: A synthesis of results from Site 504 (DSDP legs 69, 70, and 83, and ODP legs 111, 137, 140, and 148). Proc. Ocean Drill. Program Sci. Results, 148: 417-434, doi:10.2973/odp.proc. sr.148.159.

Ayadi M., Pezard P., Tartarotti P., Bronner G. and Laverne C., 1998. Multi scalar structure at DSDP/ODP site 504, Costa Rica Rift, III: faulting and fluid circulation. Constraints from integration of FMS images, geophysical logs and core data. Geol. Soc. London Spec. Publ., 136: 1-326.

Bach W., Peucker-Ehrenbrink B., Hart S.R. and Blusztajn J.S., 2003. Geochemistry of hydrothermally altered oceanic crust: DSDP/ODP Hole 504B - Implications for seawater-crust exchange budgets and Sr- and Pb-isotopic evolution of the mantle. Geochem. Geophys. Geosyst., 4: 8904, doi:10.1029/2002 GC000419.

Bohnenstiehl D.R. and Carbotte S.M., 2001. Faulting patterns near 19,30°S on the East Pacific Rise: Fault formation and growth at a superfast-spreading center. Geochem. Geophys. Geosyst., 2: 1056, doi:10.1029/2001GC000156.

Carbotte S.M. and Macdonald K.C., 1990. Causes of variation in fault-facing direction on the ocean floor. Geology, 18: 749-752. doi:10.1130/0091-7613(1990)018<0749:COVIFF>2.3.CO;2

Carbotte S.M. and Macdonald K.C., 1994a.The axial topographic high at intermediate and fast spreading ridges. Earth Planet. Sci. Lett., 128: 85-97. doi:10.1016/0012-821X(94)90137-6

Carbotte S.M. and Macdonald K.C., 1994b. Comparison of seafloor tectonic fabric at intermediate, fast, and super fast spreading ridges: Influence of spreading rate, plate motions, and ridge segmentation on fault patterns. J. Geophys. Res., 99: 13609-13633. doi:10.1029/93JB02971

Carbotte S.M., Ryan W.B.F., Jin W., Cormier M.H., Bergmanis E., Sinton J. and White S., 2003. Magmatic subsidence of the East Pacific Rise (EPR) at 18_140S revealed through fault restoration of ridge crest bathymetry. Geochem. Geophys. Geosyst., 4: 1008. doi:10.1029/2002GC000337

Carlson R.L., 2010. How crack porosity and shape control seismic velocities in the upper oceanic crust: Modeling downhole logs from Holes 504B and 1256D. Geochem. Geophys. Geosyst., 11: Q04007. doi:10.1029/2009GC002955

Carlson R.L., 2011. The effect of hydrothermal alteration on the seismic structure of the upper oceanic crust: Evidence from Holes 504B and 1256D, Geochem. Geophys. Geosyst., 12: Q09013. doi:10.1029/2011GC003624

Edmond J.M., Van Damm K.L. and MacDuff R.E., 1982. Measures C I. Chemistry of hot springs on the East Pacific Rise and their effluent dispersal. Nature, 297: 187-191. doi:10.1038/297187a0

Ekström M.P., Dahan C., Chen M-Y., Lloyd P. and Rossi D.J., 1987. Formation imaging with microelectrical scanning arrays. Log Analyst, 28:294-306.

Fontana E., Iturrino G.J. and Tartarotti P., 2010. Depth-shifting and orientation of core data using a core-log integration approach: A case study from ODP-IODP Hole 1256D. Tectonophysics, 494: 85-100. doi:10.1016/j.tecto.2010.09.006

France L., Ildefonse B. and Koepke J., 2009. Interactions between magma and hydrothermal system in Oman ophiolite and in IODP Hole 1256D: Fossilisation of a dynamic melt lens at fast spreading ridges. Geochem. Geophys. Geosyst., 10: Q10O19. doi:10.1029/2009GC002652.

Francheteau J. and Ballard R.D., 1983. The East Pacific Rise near 21°N, 13°N and 20°S: Inferences for along-strike variability of axial processes of the mid-ocean ridge, Earth Planet. Sci. Lett., 64: 93-116. doi:10.1016/0012-821X(83)90055-9

Gilbert L.A. and Salisbury M.H., 2011. Oceanic crustal velocities from laboratory and logging measurements of Integrated Ocean Drilling Program Hole 1256D. Geochem. Geophys. Geosyst., 12: Q09001. doi:10.1029/2011GC003750

Gillis K.M., 2002. The root zone of an ancient hydrothermal system exposed in the Troodos ophiolite, Cyprus. J. Geol., 110: 57-74. doi:10.1086/324205.

Gillis K.M., 2008. The roof of an axial magma chamber: a horn-felsic heat exchanger. Geology, 36, 299-302. doi:10.1130/g24590a.1.

Gillis K.M. and Sapp K., 1997. Distribution of porosity in a section of upper oceanic crust exposed in the Troodos Ophiolite. J. Geophys. Res., 102: 10133-10148. doi:10.1029/96JB03909

Guérin G., Goldberg D.S. and Iturrino G.J., 2008. Velocity and attenuation in young oceanic crust: new downhole log results from DSDP/ODP/IODP Holes 504B and 1256D. Geochem. Geophys. Geosyst., 9: Q12014. doi:10.1029/2008GC002203.

Hallenborg E., Harding A.J., Kent G.M. and Wilson D.S., 2003. Seismic structure of 15 Ma oceanic crust formed at an ultrafast spreading East Pacific Rise: Evidence for kilometer-scale fracturing from dipping reflectors. J. Geophys. Res., 108: 2532. doi:10.1029/2003JB002400.

Hooft E.E.E., Schouten O. and Detrick R., 1996. Constraining crustal emplacement process from the variation in seismic layer 2A thickness at east pacific rise. Earth Planet. Sci. Lett., 142: 289-309. doi:10.1016/0012-821X(96)00101-X

Hurst S.D. and Karson J.A., 2004. Side-scan sonar along the north wall of the Hess Deep Rift: Processing, texture analysis, and geologic ground truth on an oceanic escarpment. J. Geophys. Res., 109: B02107. doi:10.1029/2002jb002116|10.1029/2002jb002116

Hurst S.D, Karson J.A. and Verosub K.L., 1994. Paleomagnetism of tilted dikes in fast spread oceanic crust exposed in the Hess Deep Rift - Implications for spreading and rift propagation. Tectonics, 13: 789-802. doi:10.1029/94tc00845

Ildefonse B. and Pezard P., 2001. Electrical properties of slow-spreading ridge gabbros from ODP Site 735, Southwest Indian Ridge. Tectonophysics, 33: 69-92. doi:10.1016/S0040-1951(00)00220-1

Johnson H.P., Becker K. and Von Herzen R., 1994. Near-axis heat flow measurements on the northern Juan De Fuca Ridge: implications for fluid circulation in oceanic crust. Geophys. Res. Lett., 20: 1875-1878. doi:10.1029/93GL00734.

Karson J.A., 2002. Geologic structure of the uppermost oceanic crust created at fast- to intermediate-rate spreading centers. Ann. Rev. Earth Planet. Sci., 30: 347-384. doi:10.1146/annurev.earth.30.091201.141132

Karson J.A., Hurst S.D. and Lonsdale P., 1992. Tectonic rotations of dikes in fast-spread oceanic crust exposed near Hess Deep. Geology, 20: 685-688. doi:10.1130/0091-7613

Karson J.A., Klein E.M., Hurst S.D., Lee C.E., Rivizzigno P.A., Curewitz D., Morris, A.R. and Hess Deep '99 Scientific Party, 2002a. Structure of uppermost fast-spread oceanic crust exposed at the Hess Deep Rift: implications for subaxial processes at the East Pacific Rise. Geochem. Geophys. Geosyst., 3: 1002. doi:10.1029/2001GC000155.

Karson J.A., Tivey M.A. and Delaney J.R., 2002b. Internal structure of uppermost oceanic crust along the Western Blanco Transform Scarp: Implications for subaxial accretion and deformation at the Juan de Fuca Ridge. J. Geophys. Res., 107: 2181. doi:10.1029/2000JB000051.

Koepke J., Christie D.M., Dziony W., Holtz F., Lattard D., Maclennan J., Park S., Scheibner B., Yamasaki T. and Yamazaki S., 2008. Petrography of the Dike-Gabbro transition at IODP site 1256 (equatorial Pacific): the evolution of the granoblastic dike. Geochem. Geophys. Geosyst., 9. doi:10.1029/2008GC001939.

Koepke J., France L., Mueller T., Faure F., Goetze N., Dziony W. and Ildefonse B., 2011. Gabbros from IODP Site 1256, equatorial Pacific: Insight into axial magma chamber processes at fast spreading ocean ridges. Geochem. Geophys. Geosyst., 12: Q09014. doi:10.1029/2011gc003655

Koschinsky A., Garbe-Schönberg D., Sander S., Schmidt K., Gennerich H.H. and Strauss H., 2008. Hydrothermal venting at pressure-temperature conditions above the critical point of seawater, 5°S on the Mid-Atlantic Ridge. Geology, 36: 615-618. doi:10.1130/G24726A.1

Lister C.R.B., 1974. On the penetration of water into hot rock. Geophys. J. R. Astron. Soc., 39: 465-509. doi:10.1111/j.1365-246X.1974.tb05468.x

Lister C.R.B., 1980. Heat flow and hydrothermal circulation. Ann. Rev. Earth Planet. Sci., 8: 95-117. doi:10.1146/annurev.ea.08.050180.000523

Macdonald K.C., 1982. Mid-ocean ridges: Fine scale tectonic, volcanic and hydrothermal processes within the plate boundary zone. Ann. Rev. Earth Planet. Sci., 10: 155-90. doi:10.1146/annurev.ea.10.050182.001103

Morgan J. and Chen Y.J., 1993. The genesis of oceanic crust–magma injection, hydrothermal cooling, and crustal flow. J. Geophys. Res., 98: 6283-6297. doi:10.1029/92JB02650.

Morton J.L. and Sleep N.H., 1985. A mid-ocean ridge thermal model: constraints on the volume of axial hydrothermal heat flux. J. Geophys. Res., 90: 11345-11353. doi:10.1029/JB090iB13p11345

Nehlig P., 1993. Interactions between magma chambers and hydrothermal systems: Oceanic and ophiolitic constraints. J. Geophys. Res., 98: 19,621-19,633. doi:10.1029/93JB01822.

Nehlig P. and Juteau T., 1988. Deep seawater penetration and circulation at ocean ridges: evidence from the Oman ophiolite. Marine Geol., 84: 29-228. doi:10.1016/0025-3227(88)90102-8

Nehlig P., Juteau T., Bendel V. and Cotten J., 1994. The root zones of oceanic hydrothermal systems: Constraints from the Samail ophiolite (Oman). J. Geophys. Res., 99: 4703-4713. doi:10.1029/93JB02663.

Nicolas A., Boudier F., Koepke J., France L., Ildefonse B. and Mével C., 2008. Root zone of the sheeted dike complex in the Oman ophiolite. Geochem. Geophys. Geosyst., 9: Q05001. doi:10.1029/2007GC001918.

Palmason G., 1973. Kinematics and heat flow in volcanic rift zone, with application to Iceland. Geophys. J.R. Astron. Soc., 33: 451-481. doi:10.1111/j.1365-246X.1973.tb02379.x

Pezard P.A., 1990. Electrical properties of Mid-Ocean Ridge basalt and lmplications for the structure of the upper oceanic crust in Hole 504B. J. Geophys. Res., 95: 9237-9264. doi:10.1029/JB095iB06p09237

Pezard P.A., Lovell M. and ODP leg 126 Shiboard scientific Party, 1990. Downhole images: electrical scanning reveals the nature of subsurface oceanic crust. EOS, 71: 709-718.

Revil A. and Glover P.W.J., 1998. Nature of surface electrical conductivity in natural sands, sandstones and clays. Geophys. Res. Lett., 25: 691-694. doi:10.1029/98GL00296.

Schaefer C.J. and Kattenhorn S.A., 2004. Characterization and evolution of fractures in low-volume pahoehoe lava flows, eastern Snake River Plain, Idaho. Geol. Soc. Am. Bull., 116: 322-33. doi:10.1130/B25335.1

Serra O., 1989. Formation microscanner image interpretation. Houston (Schlumberger Educ. Services), SMP-7028.

Stein C. and Stein S., 1994. Constraints on hydrothermal heat flux through the oceanic lithosphere from global heatflow. J. Geophys. Res., 99: 3081-3095. doi:10.1029/93JB02222.

Swift S., Reichow M., Tikku A., Tominaga M. and Gilbert L., 2008. Velocity structure of upper ocean crust Formed at ODP hole 1256D. Geochem. Geophys. Geosyst., 9. doi:10.1029/2008GC002188.

Tartarotti P., Allerton S.A. and Laverne C., 1995. Vein formation mechanisms in the sheeted dike complex from Hole 504B. In: J. Erzinger, K. Becker, H.J.B. Dick and L. Stokking (Eds.), Proceed. O.D.P., Sci. Res., 137/140: 231-243. doi:10.2973/odp.proc.sr.137140.026.1995

Tartarotti P., Ayadi M., Pezard P.A., Laverne C. and de Larouzière F.D., 1998. Multi-scalar structure at DSDP/ODP Site 504, Costa Rica Rift, II: Fracturing and alteration. An integrated study from core, downhole measurements and borehole wall images. In: P.K. Harvey and M.A. Lovell (Eds), Core-Log Integration. Geol. Soc. London Spec. Publ., 136: 391-412.

Teagle D.A.H., Alt J.C., Umino S., Miyashita S., Banerjee N.R., Wilson D.S. and the Expedition 309/312 Scientists, 2006. Proc. IODP, 309/312. Washington, DC (Integrated O.D.P. Manag. Intern., Inc.). doi:10.2204/iodp.proc.309312. 2006

Teagle D.A.H., Ildefonse B., Blum P., and the Expedition 335 Scientists, 2012. Proc. IODP, 335: Tokyo (Integrated Ocean Drilling Program Management International, Inc.). doi:10.2204/iodp.proc.335.2012

Tominaga M., Teagle D.A.H., Alt J.C. and Umino S., 2009. Determination of the volcanostratigraphy of oceanic crust formed at superfast spreading ridge: Electrofacies analyses of ODP/IODP Hole 1256D. Geochem. Geophys. Geosyst., 10: Q01003. doi:10.1029/2008GC002143

Van Everdingen D.A., 1995. Fracture characteristics of the Sheeted Dike Complex, Troodos ophiolite, Cyprus: Implications for permeability of oceanic crust, J. Geophys. Res., 100: 19957-19972. doi:10.1029/95JB01575.

Violay M., Pezard P.A. and Ildefonse B., 2010. Petrophysical properties of the root zone of sheeted dikes in the ocean crust: A case study from Hole ODP/IODP 1256D, Eastern Equatorial Pacific. Tectonophysics., 493: 139-152. doi:10.1016/j.tecto.2010.07.013

Waxman M.H. and Smits L.J.M., 1968. Electrical conductivities in oil-bearing shaly sands. Soc. Petrol. Engin. J., 8: 107-122. doi:10.2118/1863-A.

Wilson D.S., 1996. Fastest known spreading on the Miocene Cocos-Pacific plate boundary. Geophys. Res. Lett., 23: 3003-3006. doi:10.1029/96GL02893

Wilson D.S., Teagle D.A.H., Alt J.C., Banerjee N.R., Umino S., Miyashita S., Acton G.D., Anma R., Barr S.R., Belghoul A., Carlut J., Christie D.M., Coggon R.M., Coope, K.M., Cordier C., Crispini L., Durand S.R., Einaudi F., Galli L., Gao Y.J., Geldmacher J., Gilbert L.A., Hayman N.W., Herrero-Bervera E., Hirano N., Holter S., Ingle S., Jiang S.J., Kalberkamp U., Kerneklian M., Koepke J., Laverne C., Vasquez H.L.L., Maclennan J., Morgan S., Neo N., Nichols H.J., Park S.H., Reichow M.K., SakuyamaT., Sano T., Sandwell R., Scheibner B., Smith-Duque C.E., Swift S.A., Tartarotti P.,Tikku A.A., Tominaga M., Veloso E.A., Yamasaki T., Yamazaki S. and Ziegler C., 2006. Drilling to gabbro in intact ocean crust. Science, 312: 1016-1020. doi:10.1126/science.1126090.